Calibration of Voyager Cosmic Ray Detectors for Magnetospheric Electrons

R. S. Selesnick and M. D. Looper

Space Radiation Laboratory
California Institute of Technology
Pasadena, California

SRL Internal Report 100

ABSTRACT

A laboratory calibration of Voyager cosmic ray (CRS) detectors for electrons in the energy range from ~0.5 to 3 MeV is described. The results are used in a calculation of the single–detector response functions. Results from separate calibrations of the instrument electronics are useful for incorporating the effects of deadtime and pulse pileup due to high electron flux.

December 14, 1989

Calibration of Voyager Cosmic Ray Detectors for Magnetospheric Electrons

R. S. Selesnick and M. D. Looper

Space Radiation Laboratory
California Institute of Technology
Pasadena, California

SRL Internal Report 100

1. Introduction

The Voyager Cosmic Ray Subsystem (CRS) has made extensive measurements of trapped, energetic particles in the magnetospheres of Jupiter, Saturn, Uranus, and Neptune. The design of each of the CRS telescopes was optimized for sensitivity to the low fluxes of interplanetary cosmic rays with energies for electrons $\geq$ 5 MeV. Magnetospheric fluxes are generally much higher, leading to a high rate of accidental coincidences among different detectors, and have soft energy spectra requiring measurements at lower energies. The data has therefore been restricted to single-detector measurements with energy thresholds of /(ap1 to 3 MeV. Reliable interpretation of these data has required a calibration of single detectors within the flight-spare CRS telescopes. In this report we describe such calibrations of the electron telescope (TET) D1 and D2 detectors and the high-energy telescope (HET) B2 detector for electrons.

The aim of the calibrations is to allow a calculation of the electron differential intensity, $j(E,\alpha)$, which is a function of kinetic energy, E, and pitch-angle, α. Here we assume that the magnetospheric electrons are gyrotropic with respect to the local magnetic field. Referring to a coordinate system with its polar axis along the symmetry axis of the telescope, α is a function of the spherical angles θ and ϕ. We define the response function, R, of a given detector by

$$N(E) = \tau \int_0^\infty \int_0^{2\pi} \int_0^{\pi} R(E,E',\theta)\, j(E',\alpha(\theta,\phi))\, \sin\theta\, d\theta\, d\phi\, dE' \qquad (1)$$

where $N(E)dE$ is the number of counts recorded by the detector at energies between E and $E+dE$ during the livetime τ. We have assumed azimuthal symmetry in R, corresponding to that of the telescope. After integrating (1) over energy ranges at which measurements are made by CRS, the equation can be inverted to find j in terms of N and R. The inversion problem will not be discussed in this report. Section 2 describes how the laboratory data necessary for constructing the response functions of the D1, D2 and B2 detectors were taken

with a β-spectrometer. Section 3 discusses the the calculation of the response function and presents results. Section 4 describes a correction due to shielding of the detectors by the rest of the Voyager spacecraft. Section 5 describes a calibration of the TET electronics module and subsequent corrections which are necessary in the analysis of data taken by CRS with high electron fluxes. An appendix lists the stored locations of calibration data.

2. Beta-spectrometer

The β–spectrometer used for these calibrations consists of an electron beam from a β–decay source whose energy is selected by a variable magnetic field prior to a collimation slit in front of the detector. For a detailed description see the report by M. Tran (SRL internal report #96). Calibrations of energy vs. magnetic field and of beam flux vs. energy were repeated prior to the detector calibrations (see β–spectrometer run log, volumes 2 and 3 in room 228 Downs). For these preliminary calibrations, and for the beam mapping described below, we used a single-detector mount that allowed the detector to be held in the electron beam so that its center remained at a fixed position (about 9" above the beam slit, and with no lateral movement) as it was tilted. Aluminum mounts were made to allow the TET and HET to be mounted at varying angles of incidence of the electron beam relative to the telescope axes. These mounts allowed the telescopes to be rotated in 10° increments about one of several axes so that we could retain the feature described above for the single-detector mount, namely that the detector's center did not move as the telescope was tilted, for each of the detectors in the telescope. Moreover, the detector in the telescope was placed in the same position as the single detector when the mounts were switched without moving the x-y positioning carriage; this allowed us to apply the single-detector beam-mapping and other calibrations directly to the telescope-detector calibrations.

To determine the uniformity of the electron beam we have measured the flux with a single bare detector at various positions relative to the slit. The distance above the slit was fixed at the value used for the TET calibrations. The detector has a radius of 12 mm and the slit has a length of 1.5" and a width of 0.5". To resolve the shape of the beam at scales smaller than the detector radius, measurements were taken with the center of the detector at approximately 10 mm intervals in both x and y. The flux (counts s^{-1}) measured at position $\mathbf{r}_i$ in the x–y plane is

$$R_i = \int d^2r\, \Theta(|\mathbf{r}-\mathbf{r}_i|) f(\mathbf{r}) \qquad (2)$$

where $f(\mathbf{r})$ is the flux density (electrons $cm^{-2}s^{-1}$) and $\Theta(r)$ is 1 for r less than the radius of the detector, 0 otherwise. With a finite number of measurements the solution of (2) for $f(\mathbf{r})$ is not unique, and some assumptions must be made. The simplest assumption is that $f(\mathbf{r})$ should

be as close as possible to some initial guess. This is enough to provide a unique solution, but it is also useful to make an additional assumption about the smoothness of $f(\mathbf{r})$. The solution can be written (see Tarantola and Valette, *Rev. Geophys. Space Phys., 20, 219–232, 1982*)

$$f(\mathbf{r}) = f_0(\mathbf{r}) + \int d^2r' \sum_{i,j} C_{f_0 f_0}(\mathbf{r},\mathbf{r}')\, \Theta(|\mathbf{r}'-\mathbf{r}_i|)\, (S^{-1})_{ij} \left\{ R_j - \int d^2r'' \, \Theta(|\mathbf{r}''-\mathbf{r}_i|) f_0(\mathbf{r}'') \right\} \quad (3)$$

where the matrix

$$S_{ij} = \int d^2r' \; d^2r'' \; \Theta(|\mathbf{r}'-\mathbf{r}_i|)\, C_{f_0 f_0}(\mathbf{r}',\mathbf{r}'')\, \Theta(|\mathbf{r}''-\mathbf{r}_j|) \quad (4)$$

The *a priori* information is represented by the flux density $f_0(\mathbf{r})$ and the correlation function $C_{f_0 f_0}(\mathbf{r},\mathbf{r}')$, which describes the smoothness of the solution. If $f_0 = 0$ and $C_{f_0 f_0}(\mathbf{r},\mathbf{r}') = \delta(\mathbf{r}-\mathbf{r}')$ then the solution has the least possible absolute norm and no correlation between adjacent points. Such a solution is shown in Figure 1a. A similar solution is shown in Figure 1b, except that Gaussian correlations are included (with a correlation length of ~2 mm) to provide smoothness. Both of the solutions in Figure 1 reproduce the data exactly. The beam is resolved at a scale roughly equal to the overlap area of the detector positions.

The results in Figure 1 are for a beam energy of 1.27 MeV. Similar measurements at other energies are consistent with approximately the same beam shape. The beam has a broad peak whose dimensions follow those of the slit, but which is divided into two local maxima, one at each end of the slit. The location chosen for the calibrations was the local minimum between these maxima, as it was expected the beam would be most uniform on the scale of the telescope detectors there. This placed the detector center approximately 44 mm to the north of the center of the beam-collimation slit at the 9" height at which measurements were made, so that when the detector axis is vertical the electron beam is incident at an angle of approximately $\theta_B = 11°$. This angle (and a 3° error in mounting the HET telescope) were taken into account in the subsequent data analysis.

Finally, since we wanted to calibrate the telescope detectors with all the absorbers and shielding present that are present in the flight units, we obtained a sample of the thermal blanket used to shroud the flight units and mounted it in a wire frame which was held by four aluminum stands set on the floor of the β-spectrometer vacuum chamber floor, so that it was between the telescope and the beam slit.

3. Response functions

The β-spectrometer calibrations were made with an electron beam whose differential intensity is given by

$$j(E,\theta,\phi) = J_b\, \delta(E-E_b) \frac{\delta(\theta-\theta_b)}{\sin\theta} \delta(\phi-\phi_b) \quad (5)$$

where J_b is the beam flux density (electrons $cm^{-2}s^{-1}$), E_b is the beam energy and the two angles, θ_b and ϕ_b, represent the beam direction. Substituting (5) into (1) and solving for R gives

$$R(E,E_b,\theta_b) = \frac{N(E)}{\tau J_b} \tag{6}$$

which we have used to calculate the response function at each beam energy and direction. N(E) is averaged over the width of the pulse-height analyzer channels (8 keV), and includes a background subtraction and a correction for the β decay of the source during the time between the measurement of the beam flux and the calibration run. Selected results for each of the D1, D2, and B2 detectors are given in Figures 2 to 6, which show plots of R versus E for particular indicated values of beam energy, E_b, and incidence angle, θ_b.

The response function calculated via (6) provides a complete description of the detector characteristics for each of the electron beam energies and directions studied. However, because it is a function of three variables it is cumbersome to use, and the inversion of (1) to find j is too time consuming for most applications. We have therefore performed integrations over the angles and energy which lead to less general, but more useful results. First we assume that the magnetospheric electrons satisfy

$$j(E,\alpha) = j_\perp(E)\sin^{2n}\alpha \tag{7}$$

which is often referred to as a "trapped" or "pancake" type distribution. The constant n can take any real, non–negative value, but we have chosen the three values $n = 0$, 1 and 2, and, substituting (7) into (1), performed the integrations over θ and ϕ. A correction for spacecraft obscuration, described in the next section, was included at this stage. The pitch angle dependence is

$$\sin^{2n}\alpha = \left[\sin^2\theta\,\cos^2\phi + (\cos\theta_B\,\sin\theta\,\sin\phi - \sin\theta_B\,\cos\theta)^2\right]^n \tag{8}$$

where θ_B is the angle from the telescope axis to the local magnetic field direction. We have chosen values of $\theta_B = 0$, 45° and 90°. Since α is independent of θ_B for $n = 0$ (the isotropic case) there are seven separate integrations. The result is seven new response functions which depend on E and $E' = E_b$ only. Each response function was then replaced by a smooth curve using an FFT low-pass filter (see Press et al., *Numerical Recipes, Ch. 13, Cambridge University Press, 1986*). Results of this procedure are shown in Figures 7 and 8, where the D1 integrated response functions for a beam energy of 2.36 MeV, are plotted versus E for $n = 0$ and 1 respectively. The dotted curves show the smoothed versions. After the angular integrations we performed two-dimensional cubic spline interpolation to fill in the energies between values of E' at which the calibrations were made, and obtain the response functions in the

form of two-dimensional arrays with regular spacing in each direction. The results for the three detectors, D1, D2 and B2, are shown for the isotropic case in Figure 9, 10, and 11. These are three dimensional plots with E and E' along the x and y-axes, and R along the z-axis. Note that the R axes have different relative scales.

Each response function has also been integrated over the incident energy, E', which leads to the energy dependent geometry factors, $A\,\Omega(E)$. These are plotted for the three detectors in Figures 12, 13, and 14. All seven cases are shown for each detector. $A\,\Omega(E)$ is useful for calculating the integral counting rate given $j_\perp$, n and θ_B.

4. Obscuration correction

The CRS telescopes are oriented so that the "viewing cones" defined by their detectors' separations and coincidence requirements are not obstructed by other parts of the CRS or the rest of the Voyager spacecraft. Since the calibrations discussed in this report are for single detectors, however, we must consider particles incident from well outside the normal viewing cones.

For the TET detectors, the CRS electronics box begins to cut into the incident flux at an incidence angle θ_0 from detector normal of 76° for D1, 65° for D2; since response is low at such large incidence angles anyway, we used a simple linear approximation to the obscuration in azimuth (around the telescope symmetry axis):

$$\phi = 6.4(\theta - \theta_0) \tag{9}$$

where θ is the angle of incidence and ϕ the obscured azimuth out of 360°.

For the HET, the situation is more complicated; the spacecraft HGA starts to block flux at 30° incidence, in addition to obscuration from the CRS electronics box starting at 44° . We modeled these absorbers as follows: the center of detector B2 is approximately at one cube-corner of the CRS electronics box (the telescope is set into a recess), so the box can be considered to block off one octant of the 4π steradians of potential look-angles. The spacecraft is represented by a cone frustum (the HGA) of 145" diameter narrowing to 70" diameter at 20" from its lip, where it meets a 45"-tall cylinder of 70" diameter (the main bus). The ranges of azimuth obscured by the box and the spacecraft are shown in Figures 15 and 16; azimuth zero is defined by the pointing direction $\hat{\pi}$ of Voyager 2's HET 1 B end and the spacecraft's $\hat{x}$ axis.

If we introduced obscuration as a "veto" on certain incidence directions (which would pass through the CRS or the spacecraft), it would show up as a dependence of the response function R on azimuthal angle ϕ in equation (9), and in calculating the integrated response functions described in section 3 we would have to use not only several representative values of n and of magnetic field incidence angle, but also several representative values of the magnetic

field azimuth. Accordingly, since simple simulations showed that the effect of magnetic field azimuth was small, at each incidence angle we used an average or "gray" obscuration, which was simply a multiplicative factor equal to the ratio of obscured azimuth to a full circle of 360°.

5. TET electronics calibration

We have performed tests on the TET electronics module to evaluate the importance of finite discriminator retrigger time, discriminator baseline shift and pulse pile-up in a high-intensity electron environment. Previous measurements of the retrigger time were made by M. Tran (SRL internal report, 1987, unnumbered). However, the pulse-height analysis was then inoperative and therefore did not allow an accurate energy measurement. This has since been fixed (D. Burke, private communication, 1989) and we have therefore repeated M. Tran's measurements. Details of the apparatus can be found in his report.

5.1. Channel/energy calibration

We first performed a calibration of the pulse-height analysis channel number versus energy. This was done with a TC 800 pulser driven externally by a EDC voltage source to supply the TET D1 input through a 50 ohm terminator and a 10.191 pF capacitor, at a frequency of 66 Hz. The voltage was varied from 4.1 to 20.7 mV in 90 steps and the channel number output from the microprocessor. The voltage-to-energy conversion is given by

$$E = (3.62\ \text{eV})\left[\frac{C}{e}\right]\left[\frac{V}{2}\right] = (0.11515\ \text{MeV})\ V \tag{10}$$

where C is the capacitance and V is the voltage in mV which is divided by 2 due to the termination. The energy of each channel was calculated by a linear least-squares fit with the result

$$E_n = (0.06559 \pm 0.00065) + (0.02055 \pm 0.00001)n\ \text{MeV} \tag{11}$$

where n is the channel number. The reduced χ^2 was 1.01 indicating a true linear variation. For comparison, the original TET D1 calibration (5/8/77), which was performed at 0°C, gave a channel width of 0.02016 MeV.

5.2. Retrigger time

The TET discriminator retrigger time was measured by triggering a detector with LED light pulses. The detector output went to the D1 input of the TET module. For details see M. Tran's report. The LEDs were supplied with two pulses of variable separation and energy. The pulse separation was varied until the second pulse triggered the discriminator 50 per cent of the time, as recorded by a TEK scope/counter using the R28 (TAN) output of the TET

module. The delay between the two pulses was then taken to be the retrigger time. To measure the energies of the two pulses, the guard (GA and GB) inputs were supplied to give the necessary coincidence requirements for either the first or second pulse to be analyzed. The results are given in table 1, which shows the retrigger time in micro-seconds for selected values of the two pulse energies.

E	0.518	0.579	0.682	0.785	1.093	1.504	1.915	2.326
0.518	69.0	72.0	72.0	72.0	71.0	78.0	80.0	85.0
0.579	52.0	52.0	52.0	52.0	52.0	54.0	55.0	56.0
0.682	38.0	39.0	39.0	39.0	38.5	38.0	39.0	40.0
0.785	12.5	12.5	12.5	12.5	12.7	13.0	18.0	26.0
1.093	12.5	12.5	12.5	12.3	11.8	11.5	11.5	11.5
1.504	12.5	12.5	12.5	12.3	11.8	11.5	11.5	11.5
1.915	12.5	12.5	12.5	12.3	11.8	11.5	11.5	11.5
2.326	12.5	12.5	12.5	12.3	11.8	11.5	11.5	11.5

Table 1: Retrigger time (μs) matrix. The list of energies (MeV) along the top refer to the first pulse and those down the side to the second pulse.

5.3. Baseline shift

The discriminator baseline shift effect, due to pulses adding to the overshoot of previous pulses, has been described by N. Gehrels (SRL internal report #80). We have measured the change in apparent energy of a pulse when it is one of a regular train of pulses. In each case the shift was small and we have therefore not performed a detailed study. For example, when a 2 kHz train of channel 70 pulses was changed to 50 kHz, the channel numbered changed to 65. Similarly channel 30 pulses shifted to channel 27 for a frequency change from 2 to 40 kHz.

5.4. Pile-up

To evaluate the importance of pulse pile-up we triggered the detector with two closely spaced pulses from the LEDs. The amplitude of each pulse was independently set to the same channel. Varying the delay between the pulses and measuring the resultant channel due to their combination in the discriminator gave a measure of the pile-up effect. Since the resultant channel is determined by the delay and the shape of the pulses, this procedure effectively measures the pulse shape. The results of two sets of measurements, with pulses independently (i.e. for a long delay) in channels 25 and 50, are shown in table 2. The resultant channel is

given as a function of the delay time. Since the pulse shapes from these two sets of measurements were roughly the same, no more data was taken. In each case the delay time at which the pulses pile up to 75 per cent of their sum is ~2.0 μs, which is therefore a measure of the amplifier shaping time.

delay (μs)	channel number	
∞	25	50
7.6	25	
7.0	24	
6.6		50
6.0	28	55
5.0		57
4.0	29	58
3.0	32	64
2.2	36	72
2.0	38	75
1.8	39	77
1.0	45	87
0.6		96
0.5	50	98

Table 2: Observed channel number for two piled-up, equal pulses separated by the time listed under "delay".

5.5. High-frequency background

A detailed study of the effects of random, high-frequency, low-amplitude pulses on the pulses observed at higher amplitudes was made for the low-energy telescopes (LETs) by N. Gehrels (SRL internal report #80). We have only roughly characterized the effects for the TET, which are generally small. The randomly spaced pulses were obtained by triggering a tail pulse generator externally with a random pulse generator. The amplitude was set at just below the TET threshold of channel 21. The average frequency of the random pulses was varied from 50 to 600 kHz and its effect on a regular, low-frequency train of pulses originally in channel 40 was measured. At 50 kHz there was no measurable effect. At 100 kHz the channel 40 pulse had moved to channels 38 to 39 due to baseline shift, with a small number of counts above channel 40 due to pile-up with the low-amplitude pulses. From 100 to 600 kHz these effects slowly increased. At 600 kHz there was about a 5 channel baseline shift and an

effective noise level (spread in channel number) of about 5 channels due to pile-up.

5.6. Retrigger time correction

The retrigger time calibration gave us a matrix τ_{ij} (see table 1), where i labels the energy of the second pulse and j labels the energy of the first pulse. The observed rate (counts per second) in TET channel i, r_i^{obs} is related to the true rate (that which would be observed if the retrigger time were zero), r_i^{true}, by

$$(r_i^{obs})^{-1} = (r_i^{true})^{-1} + \bar{\tau}_i \tag{12}$$

where $\bar{\tau}_i$ is an average retrigger time over all events which came before those in channel i. To define the average, note that for a retrigger time, τ, independent of energy, the observed integral rate , R^{obs}, is related to the true integral rate, R^{true}, by

$$R^{obs} = \frac{R^{true}}{1 + \tau R^{true}} \tag{13}$$

We now require that $R^{obs} = \sum_i r_i^{obs}$ which leads to

$$\bar{\tau}_i = \frac{\sum_j \tau_{ij} r_j^{true}}{r_i^{true}} \tag{14}$$

and finally

$$r_i^{obs} = \frac{r_i^{true}}{1 + \sum_j \tau_{ij} r_j^{true}} \tag{15}$$

5.7. Pile-up correction

The correction of true rates for pulse pile-up is difficult, but fortunately it is usually small. The calibration gave a pulse shape which we have used to perform Monte Carlo simulations of the pile-up. This was done by sampling from the input (true) spectrum and adding events with the pulse shape as a weighting function. Such a procedure is useful for simulating data when the input spectrum is known, but is impractical for use in fitting an unknown input spectrum to the data. We have therefore developed an analytic approach which gives acceptable results when the pile-up correction is small. We approximate the pulse shape by a square pulse of width $\tau = 2$ μs (the amplifier shaping time). The probability of no events occurring in channel j during the time τ is $e^{-\tau r_j}$, where r_j is the rate of such events. Then the rate of events in channel i which follow events in channel j within time τ, but with no other events in any other channel during this time, is $r_i(1-e^{-\tau r_j})e^{-\tau R}$, where R is the integral rate. The pile-

up correction to the rate in channel k has a contribution from events which would be in lower channels but pile up into k, and a negative contribution from events which would be in channel k but pile up to higher channels. Including both contributions, the rate corrected for pile-up of two events only is

$$r_k^{P2} = r_k + e^{-\tau R}\left[\sum_{i=1}^{k-1} r_i(1-e^{-\tau r_{k-i}}) - \sum_{i=1}^{N}\left[r_i(1-e^{-\tau r_k}) + r_k(1-e^{-\tau r_i})\right]\right] \qquad (16)$$

where the superscript $P2$ refers to the two-event pile-up corrected rate, and N is the total number of channels. The rate of two-event pile-ups can be combined in a similar way with the singles rate to obtain the three-event pile-up correction, and so on. Results of one Monte Carlo simulation (histogram) and two-event analytic calculation (dashed curve) are shown for comparison in Figure 17, along with the input spectrum (solid curve) used in both cases. The live-time of the simulation was 0.05 s.

Appendix – data storage

The calibration data are stored as a tarfile on an 8 mm tape in room 110 Downs and maybe on Odin (as disk space permits). Data from the PHA for a given run (i.e. fixed detector, energy, angle of incidence, etc.) are saved in a single file. The files for a day's runs are stored in a single directory odin:/data/bspec.1/*mmmdd*, where *mmmdd* is the date in the form, e.g., nov13. Dates run from 14 Sep 88 to 12 Apr 89. From sep14 to oct28 we were occupied with mapping the beta-spectrometer beam to choose a location at which to perform calibration measurements; PHA filenames in this period are typically composed of the location and/or the nominal value of the beta-spectrometer magnetic field, as for example aa850, ns1900, or bminus21. Identification of the named positions is given in the beta spectrometer logbooks (numbers 2 & 3); we eventually settled on position ns, and the last part of this time period was occupied with electronic noise reduction and energy calibration.

From oct31 to nov25 we acquired data for the TET D1 calibration, with a sample of the Voyager thermal blanket in place between the TET and the beam slot, as close as possible to TET D1. For nominal incidence angles less than or equal to 60 degrees the blanket normal was parallel to the TET axis; for greater angles of incidence the necessary steep angle was impossible to achieve, so at 70 degrees the blanket normal was 20 degrees from the TET axis and for angles the blanket normal was left close to vertical, i.e. the blanket was alongside the TET rather than in front of it. In this time period, PHA filenames are of form ns*BBBB.AAA*, where *BBBB* is the nominal value of the beta-spectrometer magnetic field (three or four digits) and *AAA* is the nominal incidence angle in degrees (two or three digits).

The dec01 directory contains various test runs at normal incidence, with the thermal blanket sample at various distances below TET D1, to check the effect of scattering of particles out of the beam. Filenames are of the same form as above, typically with a one-digit suffix. Consult the run logs for details.

From dec06 to jan09 we acquired data for the TET D2 calibration, again with the thermal blanket in place (though dec07 and dec12 contain a comparison of D1 & D2 with no blanket). As with D1, we had to put the blanket alongside the TET for the highest angles of incidence. Filenames are typically as for D1, with suffix ".2".

From jan24 to feb06 we did some checks of TET D4 at high angles of incidence with the thermal blanket alongside. Filenames are as for D1, with suffix ".4".

From feb09 to feb18 we began calibration of HET B2 at low angles of incidence with the thermal blanket sample in front of B1. Since the actual Voyager thermal blanket has thin "windows" for the HETs to look through, these data were not used in the final calibration. Filenames are of form het.b2.*BBBB*.*AA*, for *BBBB* and *AA* as above.

From feb21 to mar02 we continued calibration of HET B2, with the thermal blanket alongside the HET for angles of incidence greater than or equal to 33 degrees and omitted altogether for lesser angles. Some filenames have suffix "a" to avoid duplication of those taken earlier.

From mar06 to mar10 we redid the magnetic-field/energy calibration of the beta spectrometer, as we had discovered that the gaussmeter we were using had gotten slightly out of calibration and did not agree with itself when we switched between the two ranges we needed to use. As these measurements were made with a single detector at normal incidence (without the blanket, of course), filenames were typically of form sd.*BBBB*; this calibration was applied to the HET B2 measurements, while the old one was used for TET D1 & D2.

From mar11 to mar30 we finished the HET B2 calibration measurements.

From apr04 to apr06 we checked the effect of the wire harness by turning the HET on its back (so the nominal angle of incidence was 27 degrees rather than 33 degrees) so the harness was out of the beam path. These measurements were not used in the calibration.

From apr07 to apr12 we put the single detector back in to double-check the beam uniformity at the calibration position by taking measurements at various angles, searching for deviations from the expected simple cosine dependence of the total count rate on the incidence angle. Filenames are typically of form sd.*BBBB*.*AA*.

In all cases above, runs with the beta-spectrometer magnet turned off were needed for background subtraction, and runs with input from a precision pulser were used to check energy calibration and noise levels. The PHA files saving these runs typically had the magnetic field

value *BBBB* replaced by "bkgd" or "backgnd" in the former case, and "plsr" or "psr1" or some such in the latter. Finally, since some versions of the "compress" utility require input filenames of twelve or fewer characters length, we had to cut some filenames back after the fact (e.g. "het.b2" to "h.b2", or "1900" to "19"); it should still be clear which files represent what measurements as recorded in the run logs.

Applying background subtraction, energy calibration, and decay time since the last beam normalization run gives a differential energy response, which is stored in a plot file. Some of these are saved in odin:/data/bspec.1/plt, in subdirectories with the same *mmmdd* name as the PHA files, and with filenames typically obtained from the PHA filenames by substitution of "plt" for "het.b2" or "sd" or "ns" or whatever.

We thank Kirk Hargreaves for a great deal of help in the initial stages of the detector calibrations, and Dan Burke for his work on the TET electronics module.

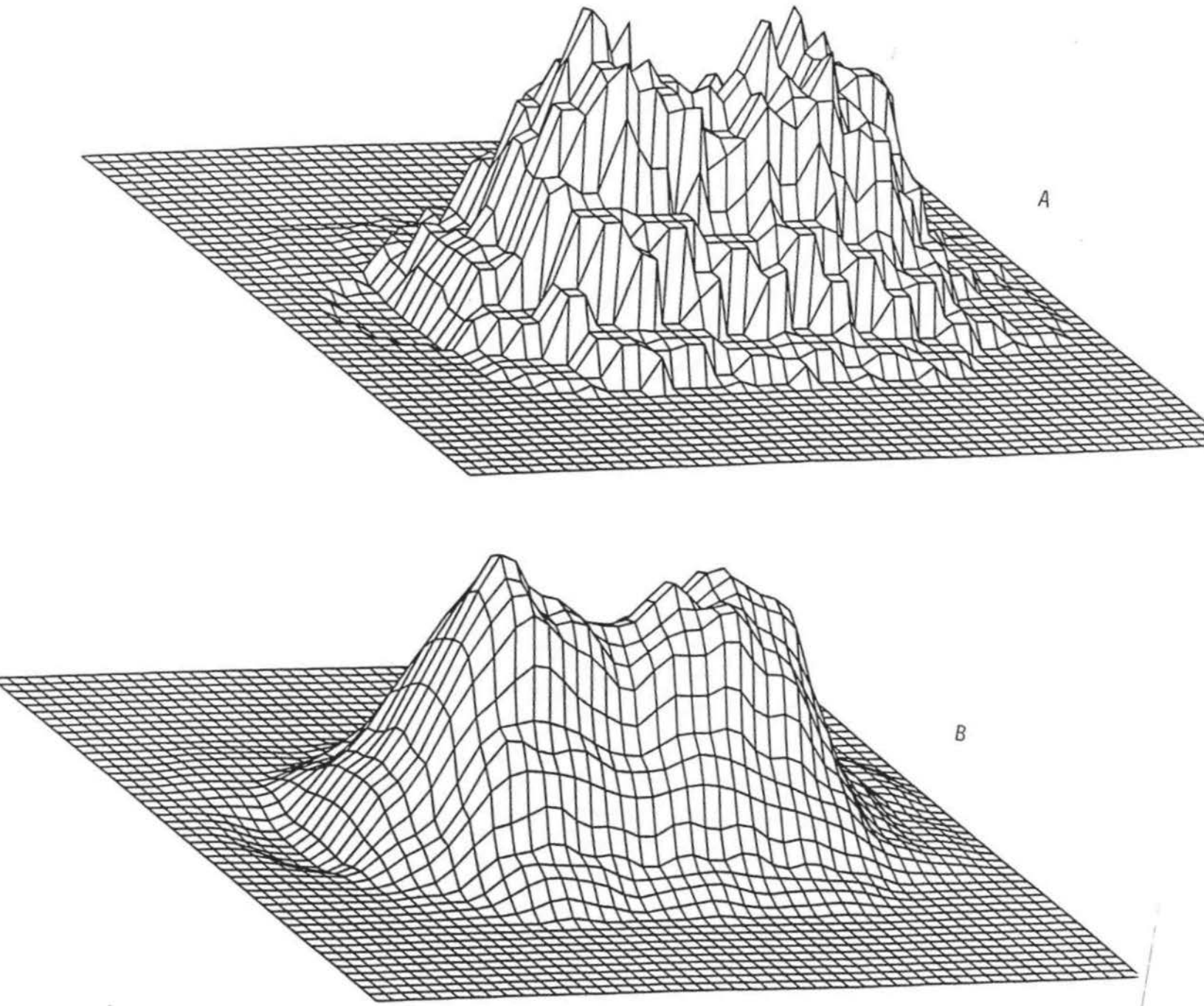

Figure 1

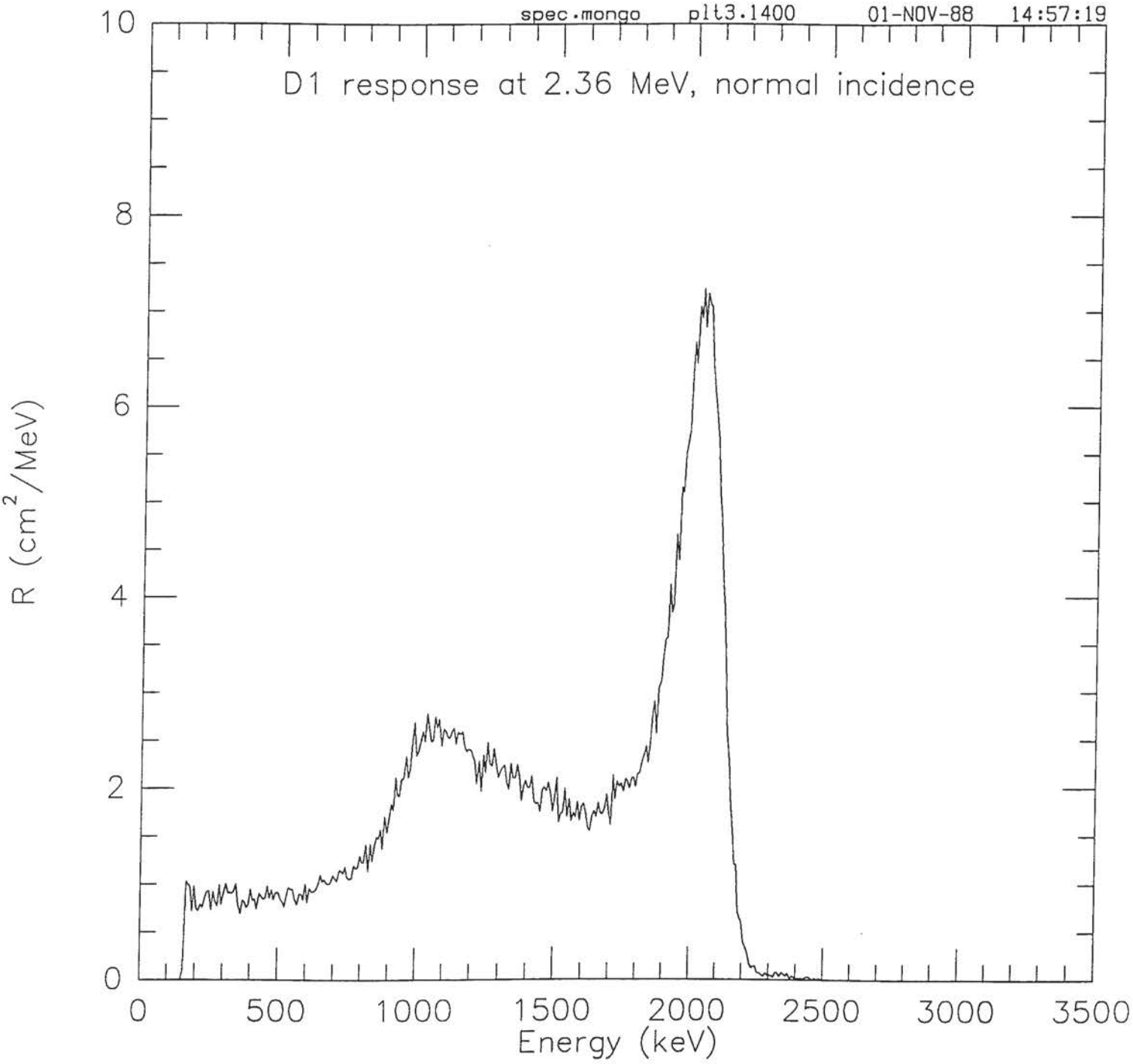
spec.mongo plt3.1400 01-NOV-88 14:57:19
D1 response at 2.36 MeV, normal incidence
R (cm²/MeV)
Energy (keV)
0
2
4
6
8
10
0
500
1000
1500
2000
2500
3000
3500

Figure 2

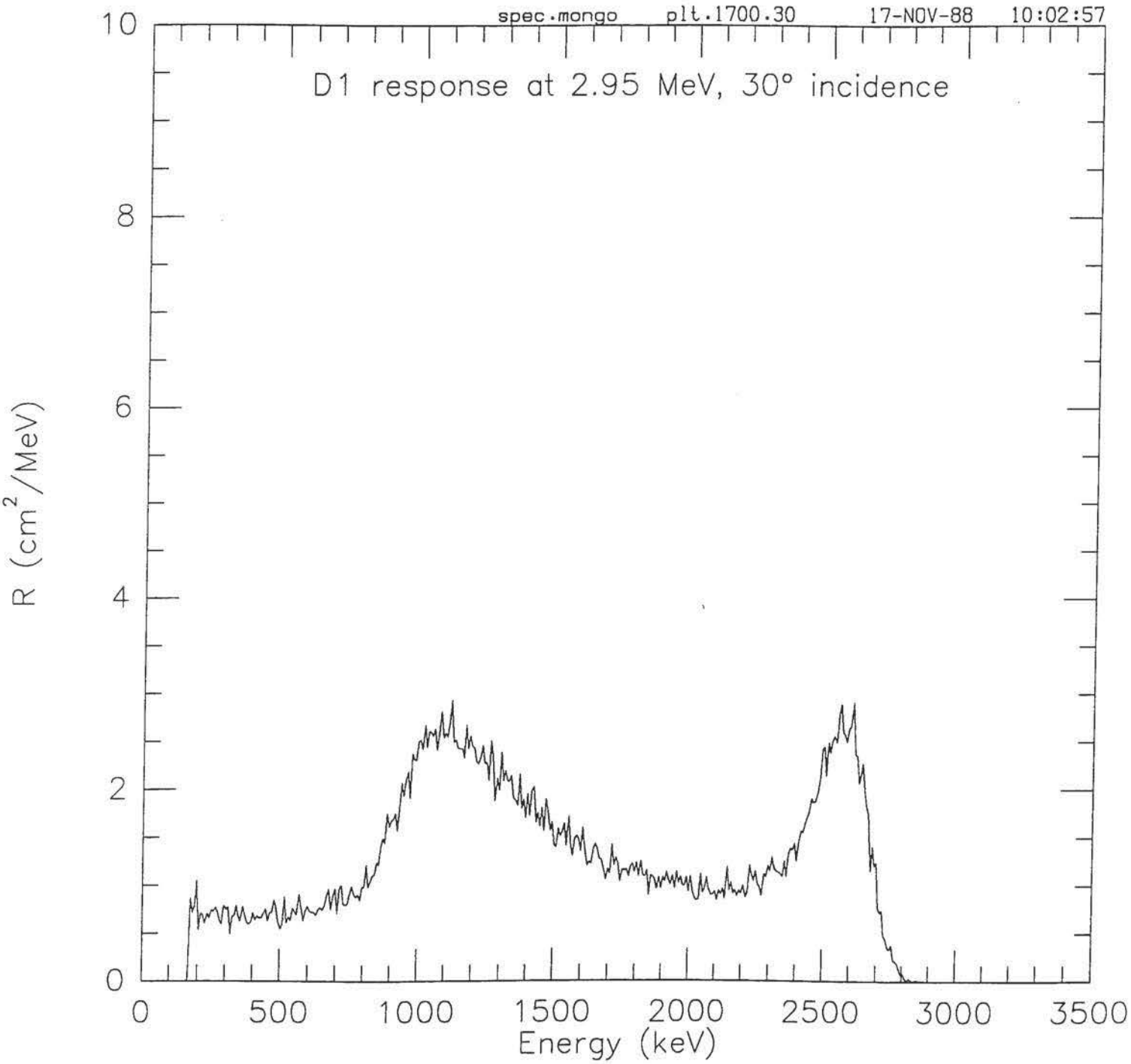
spec.mongo plt.1700.30 17-NOV-88 10:02:57
D1 response at 2.95 MeV, 30° incidence
R (cm²/MeV)
Energy (keV)
0
2
4
6
8
10
0
500
1000
1500
2000
2500
3000
3500

Figure 3

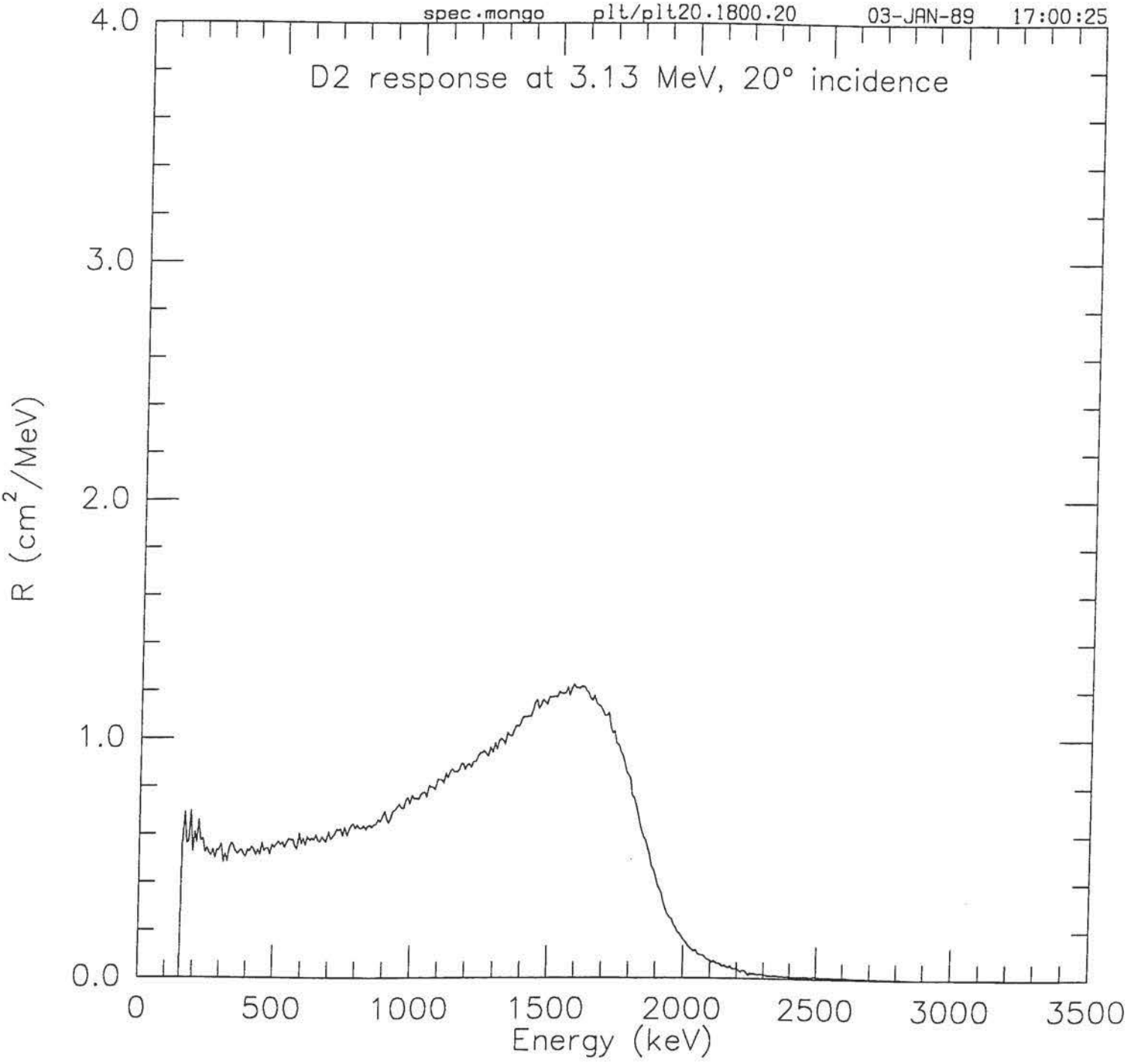
spec.mongo plt/plt20.1800.20 03-JAN-89 17:00:25
D2 response at 3.13 MeV, 20° incidence
R (cm²/MeV)
4.0
3.0
2.0
1.0
0.0
0
500
1000
1500
2000
2500
3000
3500
Energy (keV)

Figure 4

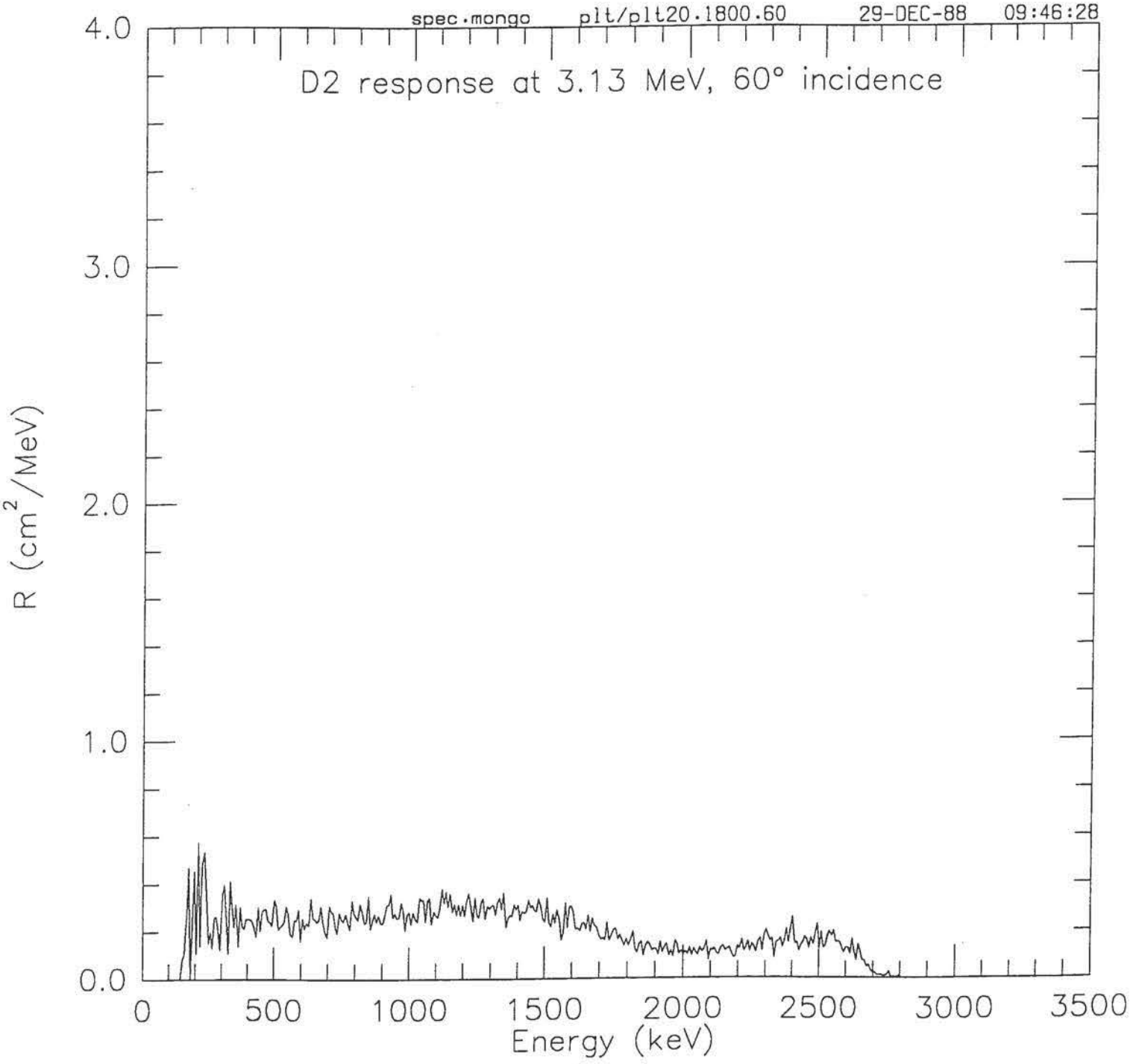
spec.mongo plt/plt20.1800.60 29-DEC-88 09:46:28
D2 response at 3.13 MeV, 60° incidence
R (cm²/MeV)
4.0
3.0
2.0
1.0
0.0
0
500
1000
1500
2000
2500
3000
3500
Energy (keV)

Figure 5

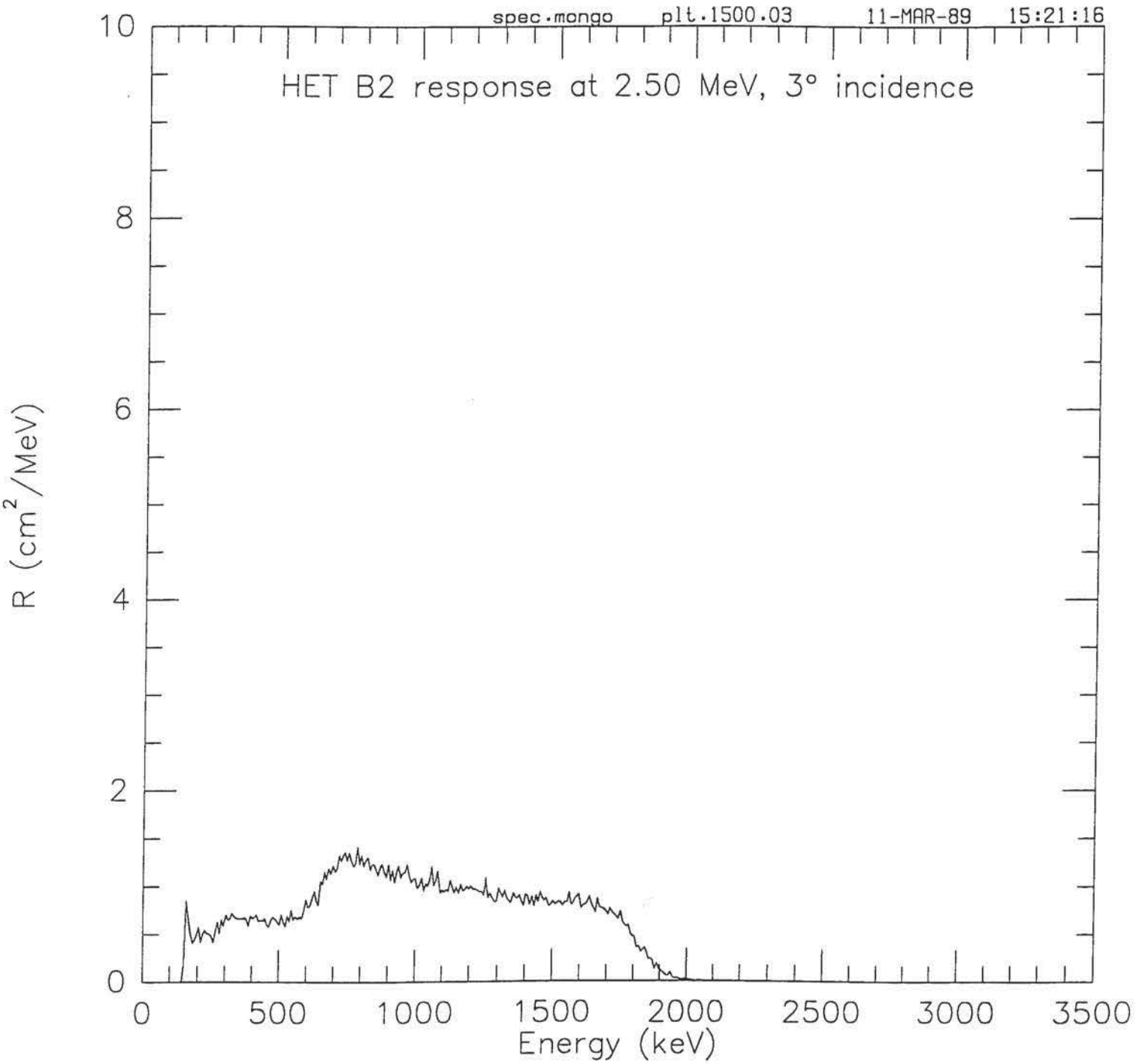
spec.mongo plt.1500.03 11-MAR-89 15:21:16
HET B2 response at 2.50 MeV, 3° incidence
R (cm²/MeV)
Energy (keV)
0
2
4
6
8
10
0
500
1000
1500
2000
2500
3000
3500

Figure 6

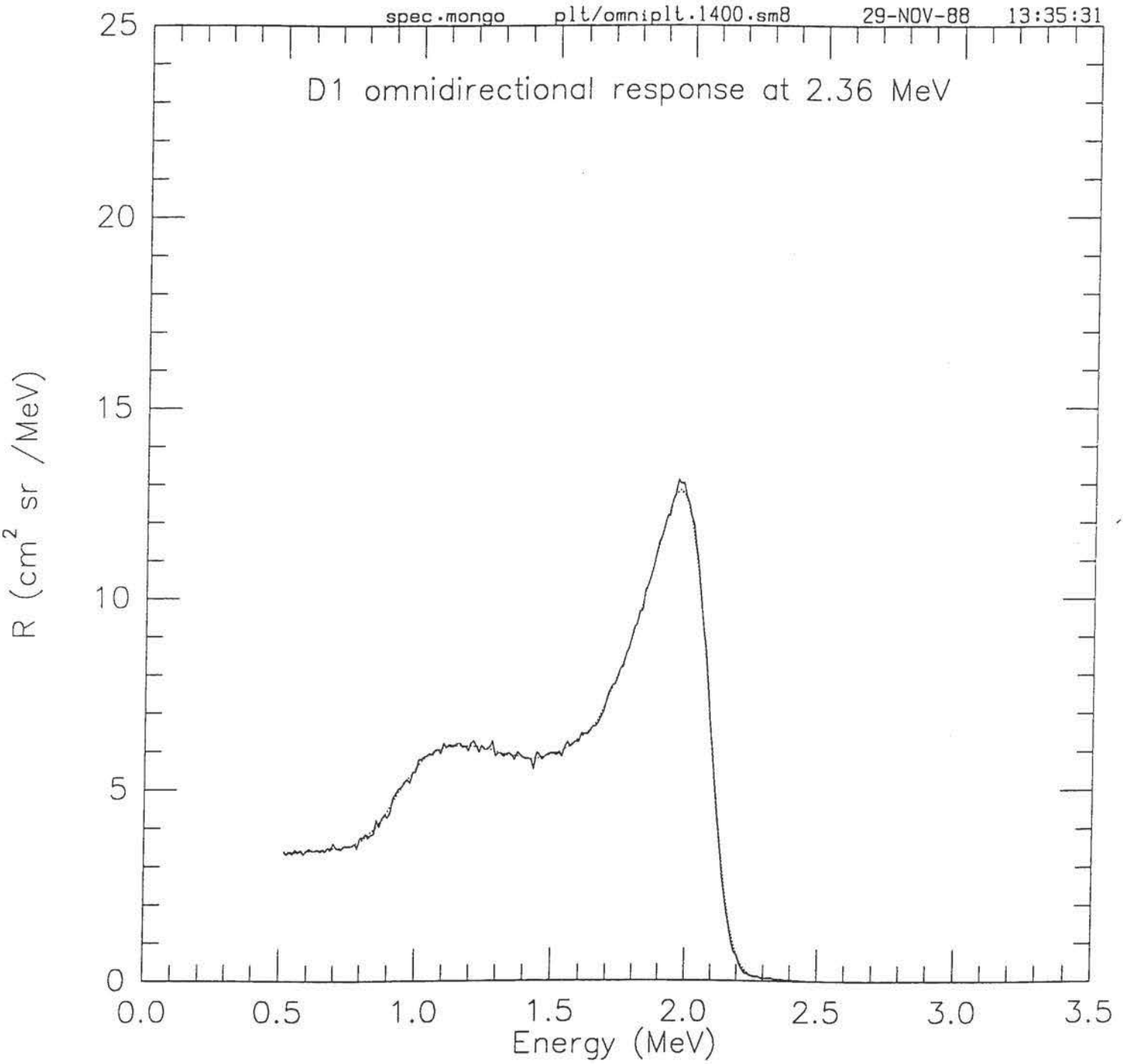
spec.mongo plt/omniplt.1400.sm8 29-NOV-88 13:35:31
D1 omnidirectional response at 2.36 MeV
R (cm^2 sr /MeV)
Energy (MeV)
0
5
10
15
20
25
0.0
0.5
1.0
1.5
2.0
2.5
3.0
3.5

Figure 7

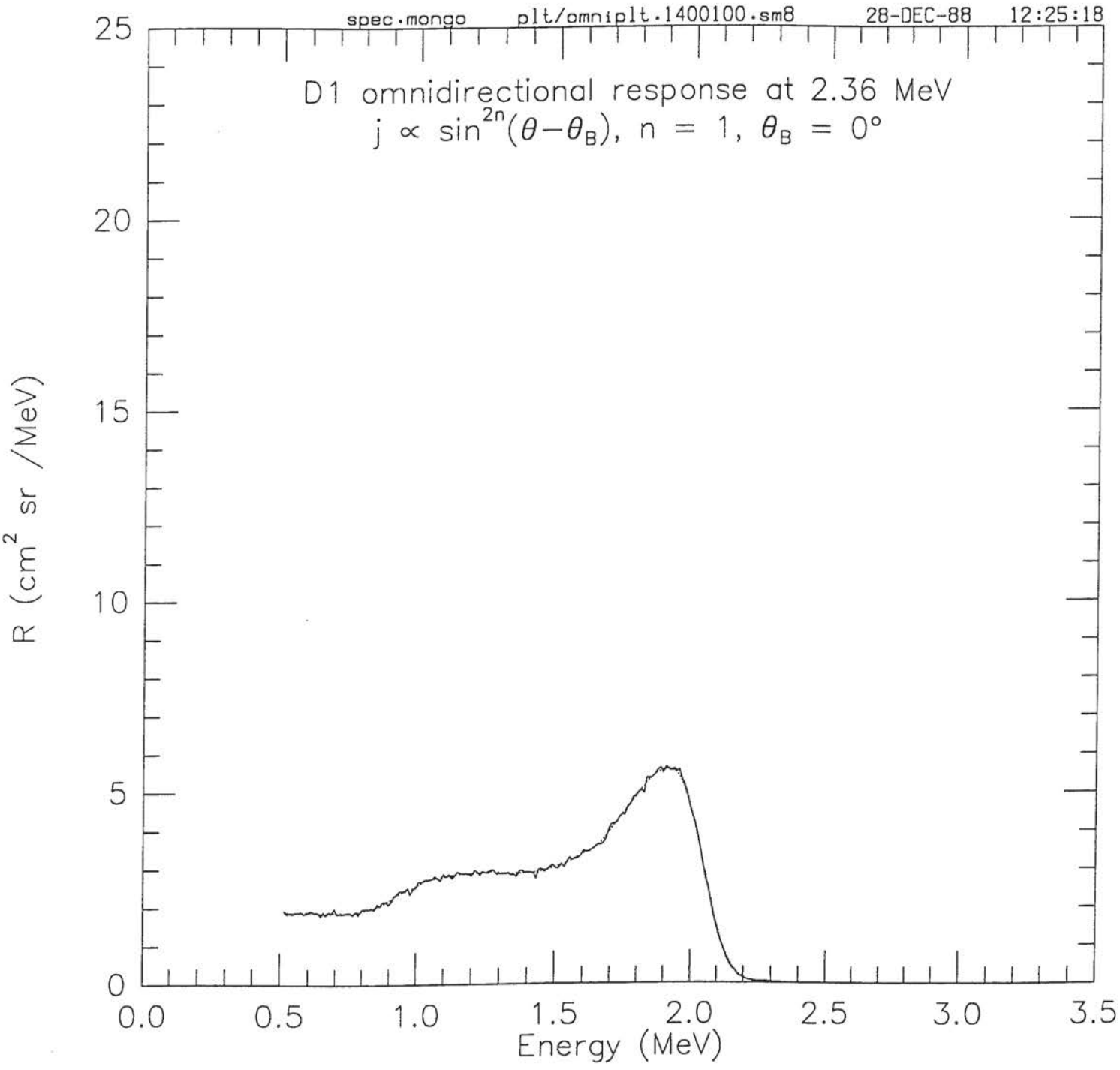
spec.mongo plt/omniplt.1400100.sm8 28-DEC-88 12:25:18
D1 omnidirectional response at 2.36 MeV
j ∝ sin^2n(θ−θB), n = 1, θB = 0°
R (cm^2 sr /MeV)
Energy (MeV)
0
5
10
15
20
25
0.0
0.5
1.0
1.5
2.0
2.5
3.0
3.5

Figure 8

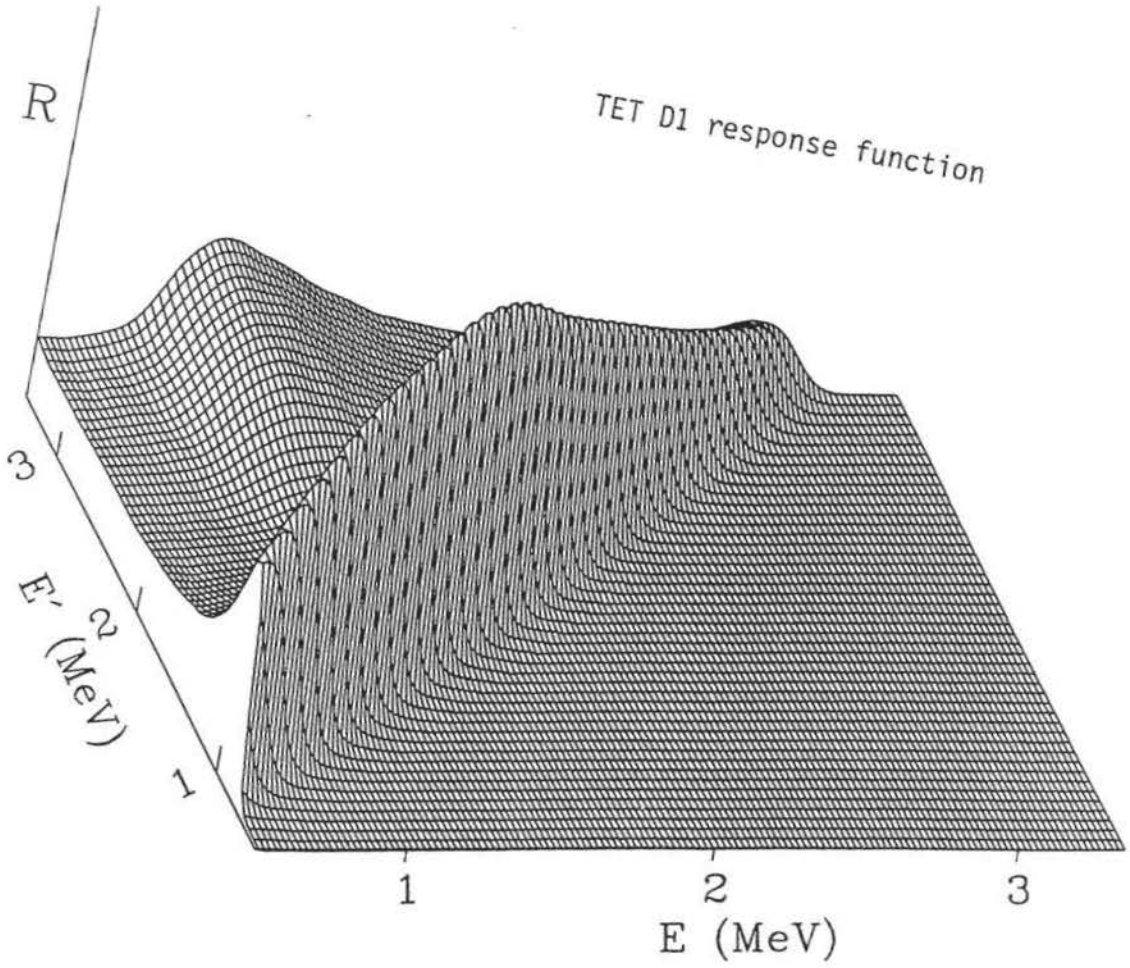

Figure 9

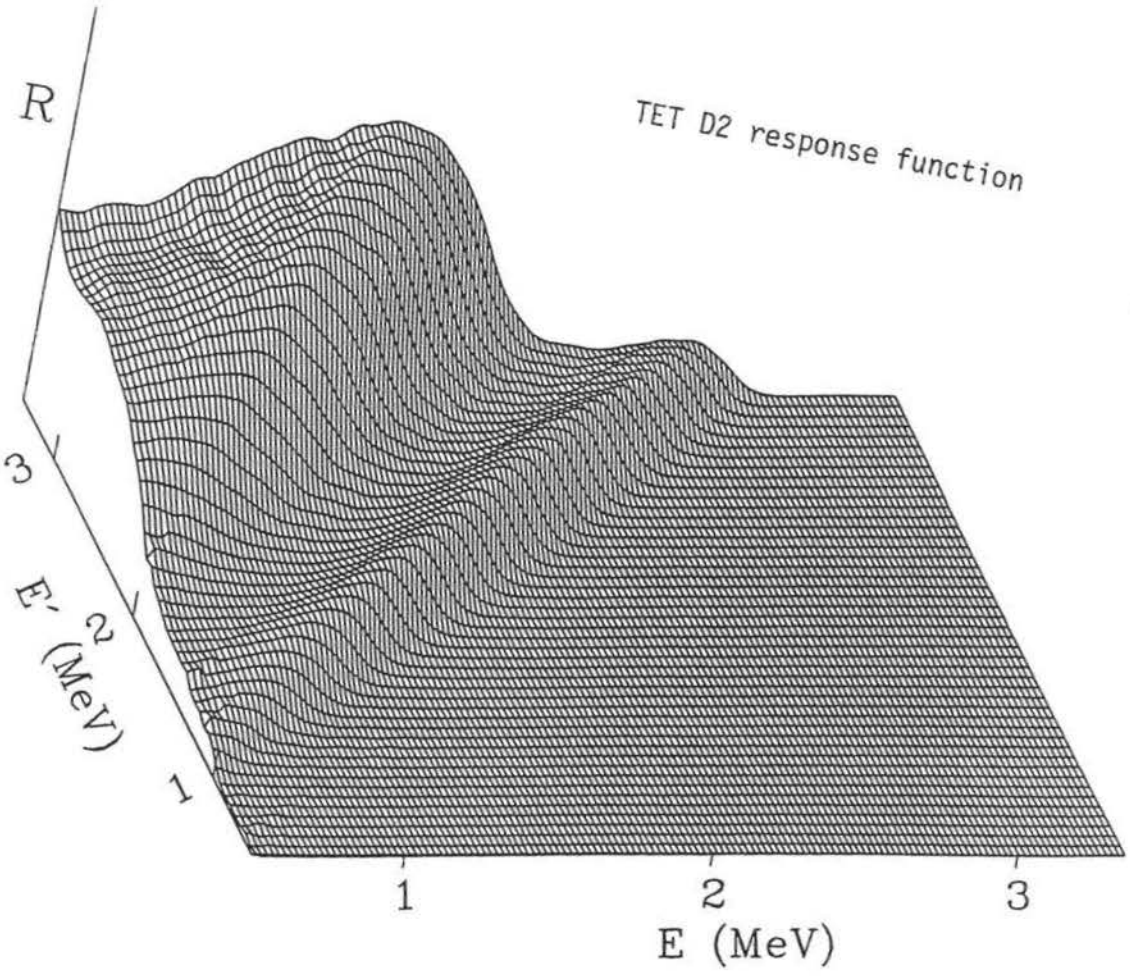

Figure 10

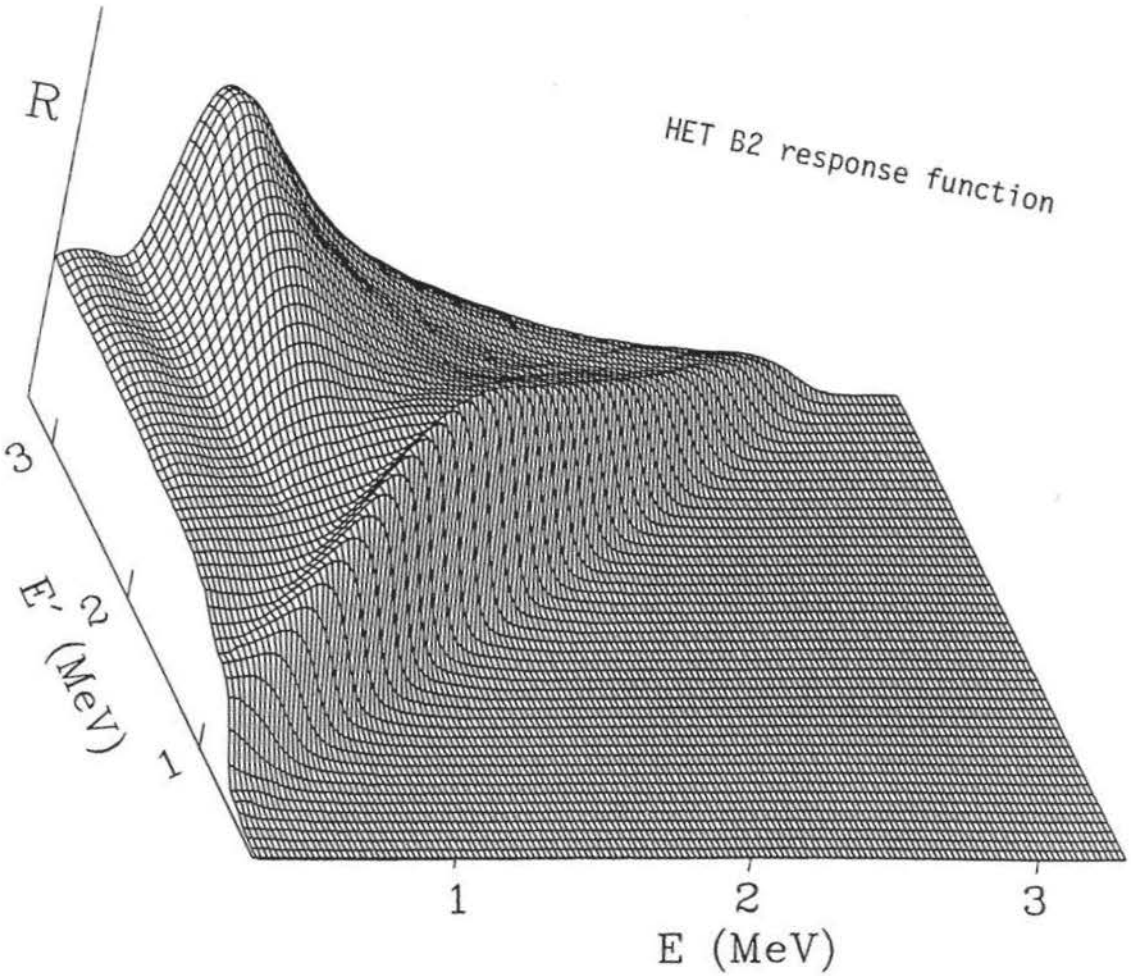

Figure 11

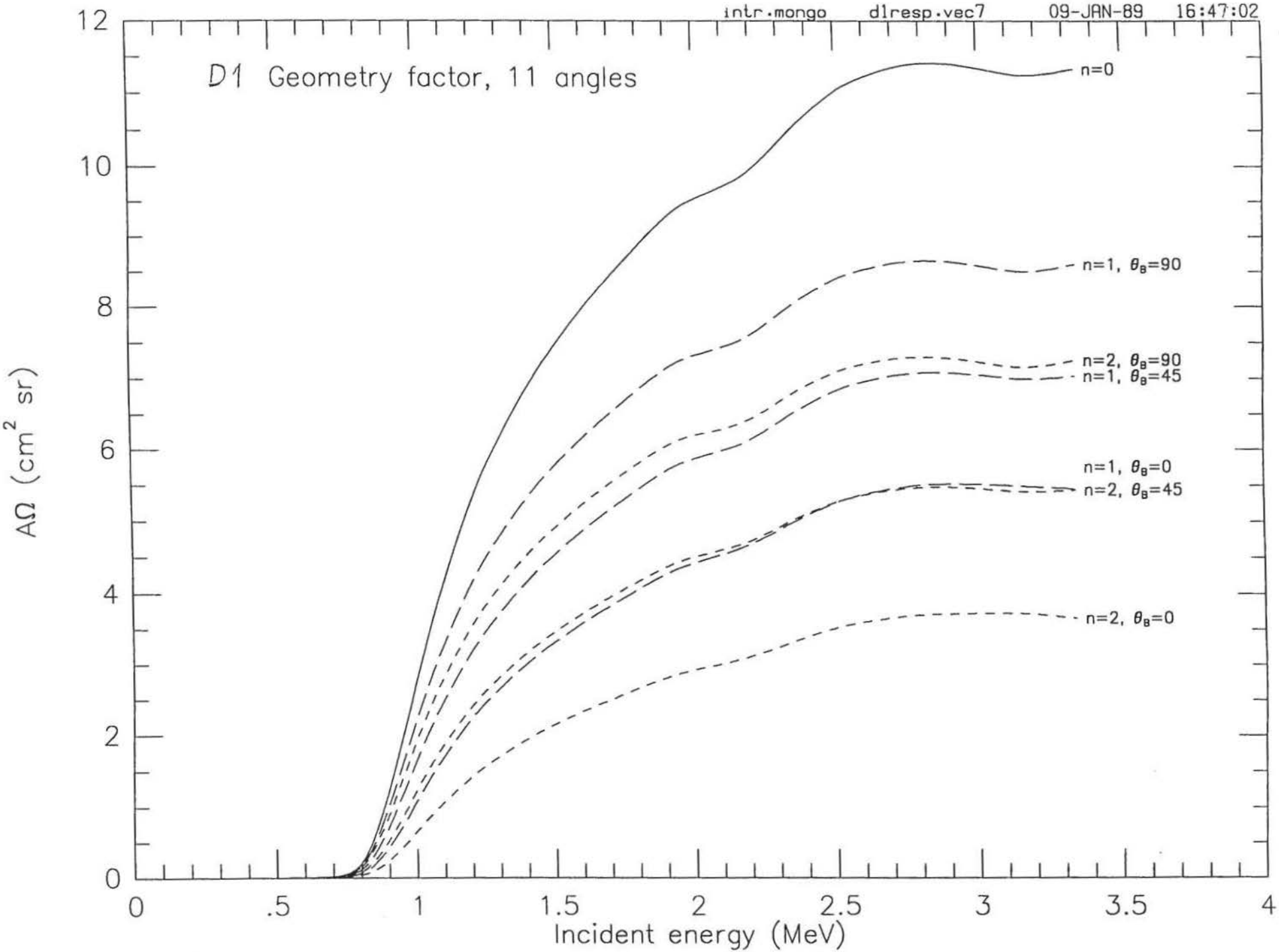
intr.mongo dlresp.vec7 09-JAN-89 16:47:02
D1 Geometry factor, 11 angles
n=0
n=1, θB=90
n=2, θB=90
n=1, θB=45
n=1, θB=0
n=2, θB=45
n=2, θB=0
AΩ (cm2 sr)
Incident energy (MeV)
0
2
4
6
8
10
12
0
.5
1
1.5
2
2.5
3
3.5
4

Figure 12

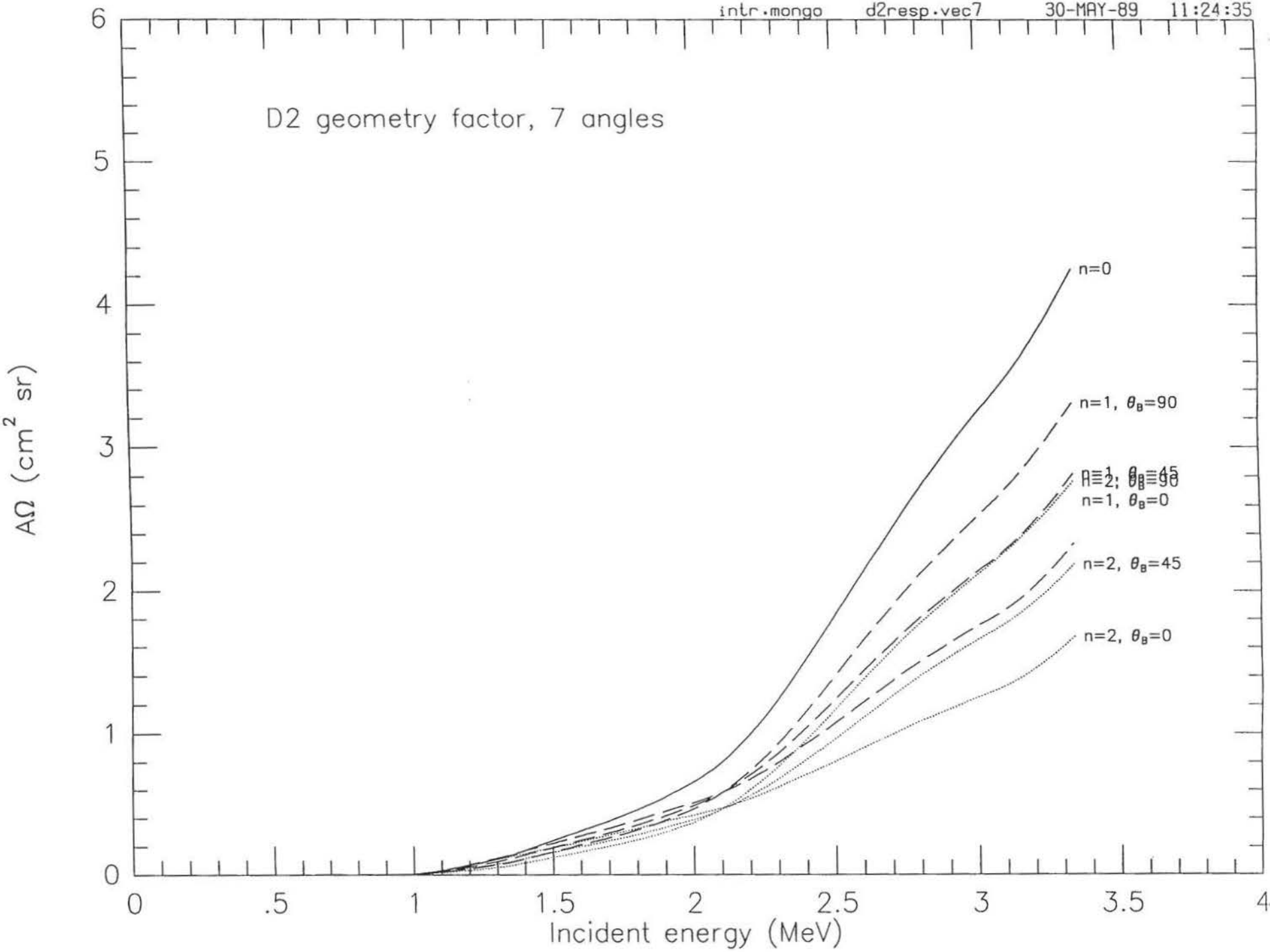
intr.mongo d2resp.vec7 30-MAY-89 11:24:35
D2 geometry factor, 7 angles
AΩ (cm² sr)
Incident energy (MeV)
n=0
n=1, θB=90
n=1, θB=45
n=2, θB=90
n=1, θB=0
n=2, θB=45
n=2, θB=0
0
.5
1
1.5
2
2.5
3
3.5
4
5
6

Figure 13

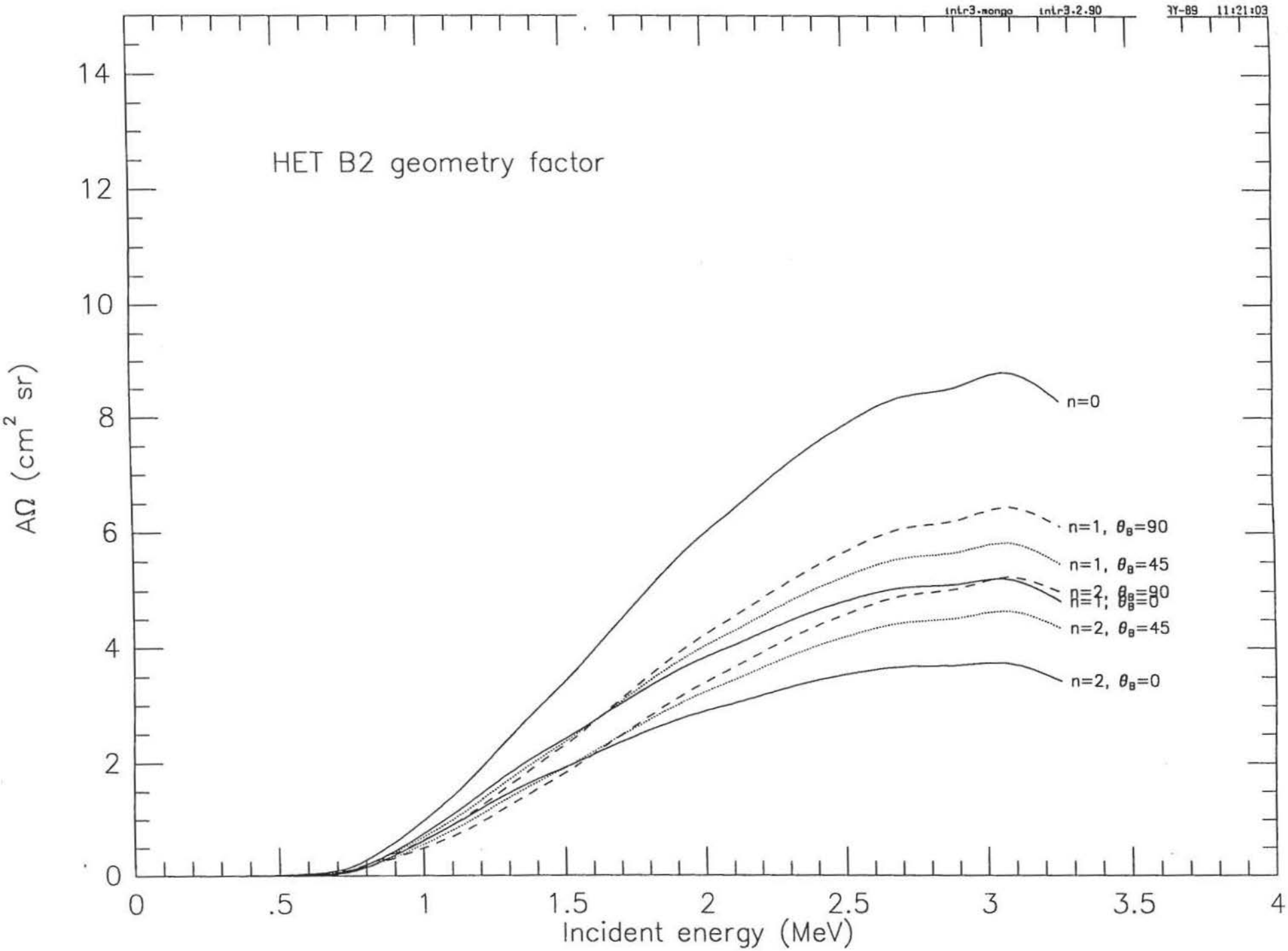
intr3-mongo intr3.2.90 7Y-89 11:21:03
HET B2 geometry factor
AΩ (cm² sr)
Incident energy (MeV)
0
2
4
6
8
10
12
14
0
.5
1
1.5
2
2.5
3
3.5
4
n=0
n=1, θB=90
n=1, θB=45
n=2, θB=90
n=1, θB=0
n=2, θB=45
n=2, θB=0

Figure 14

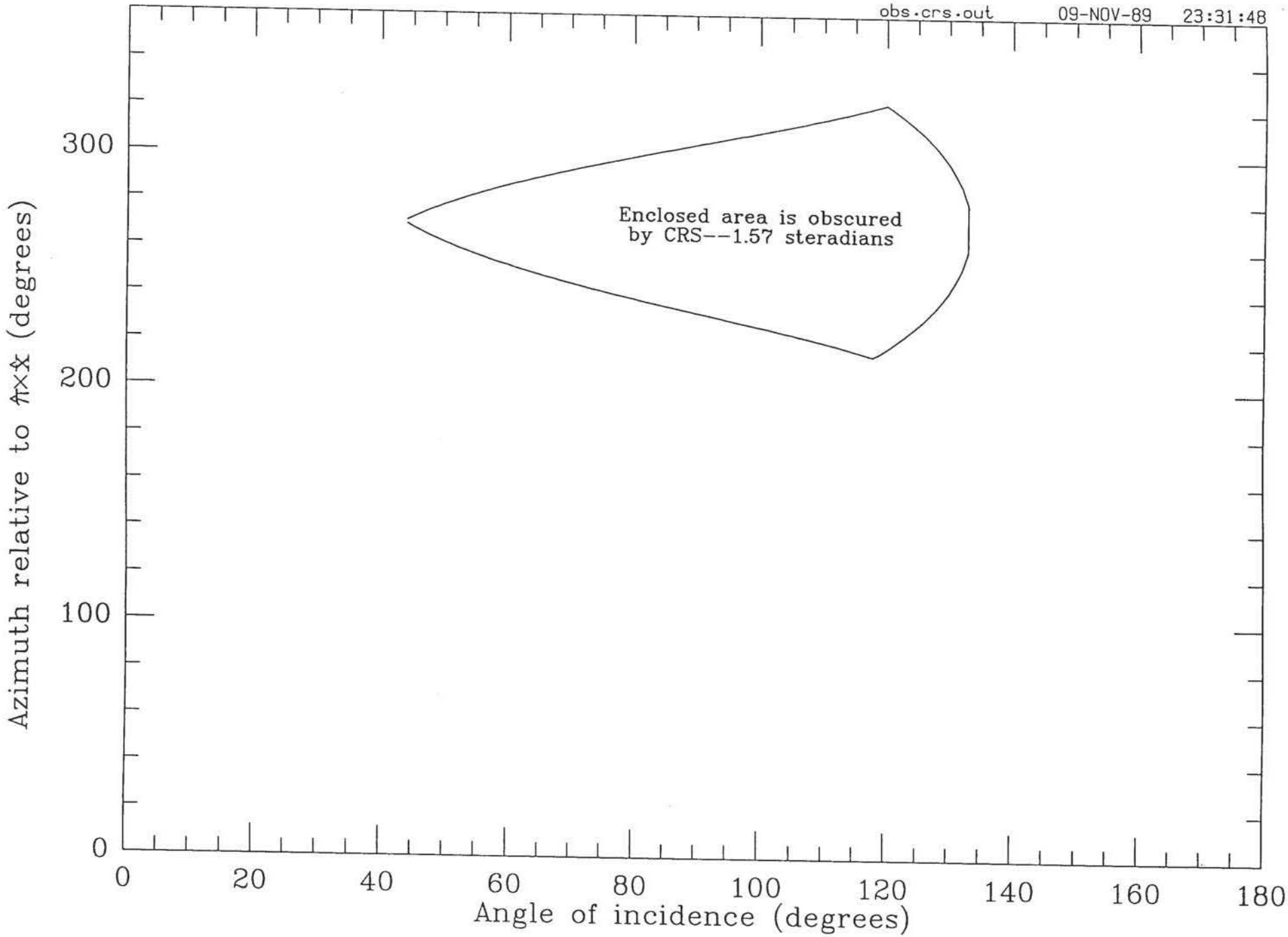
obs.crs.out
09-NOV-89
23:31:48
Enclosed area is obscured
by CRS--1.57 steradians
Azimuth relative to ATX (degrees)
0
100
200
300
0
20
40
60
80
100
120
140
160
180
Angle of incidence (degrees)

Figure 15

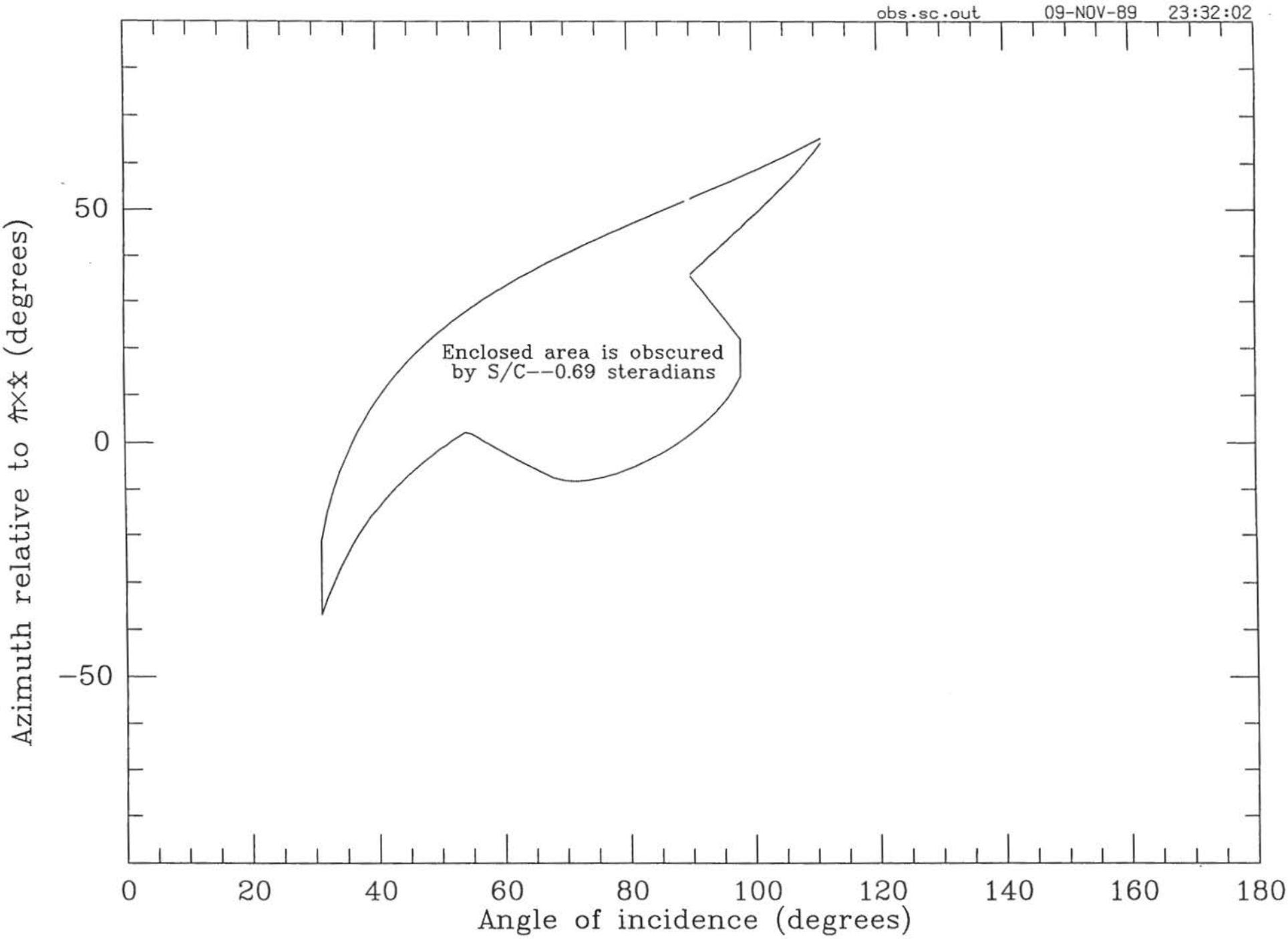
obs.sc.out 09-NOV-89 23:32:02
Enclosed area is obscured
by S/C--0.69 steradians
Azimuth relative to ⊼×⊻ (degrees)
50
0
-50
0
20
40
60
80
100
120
140
160
180
Angle of incidence (degrees)

Figure 16

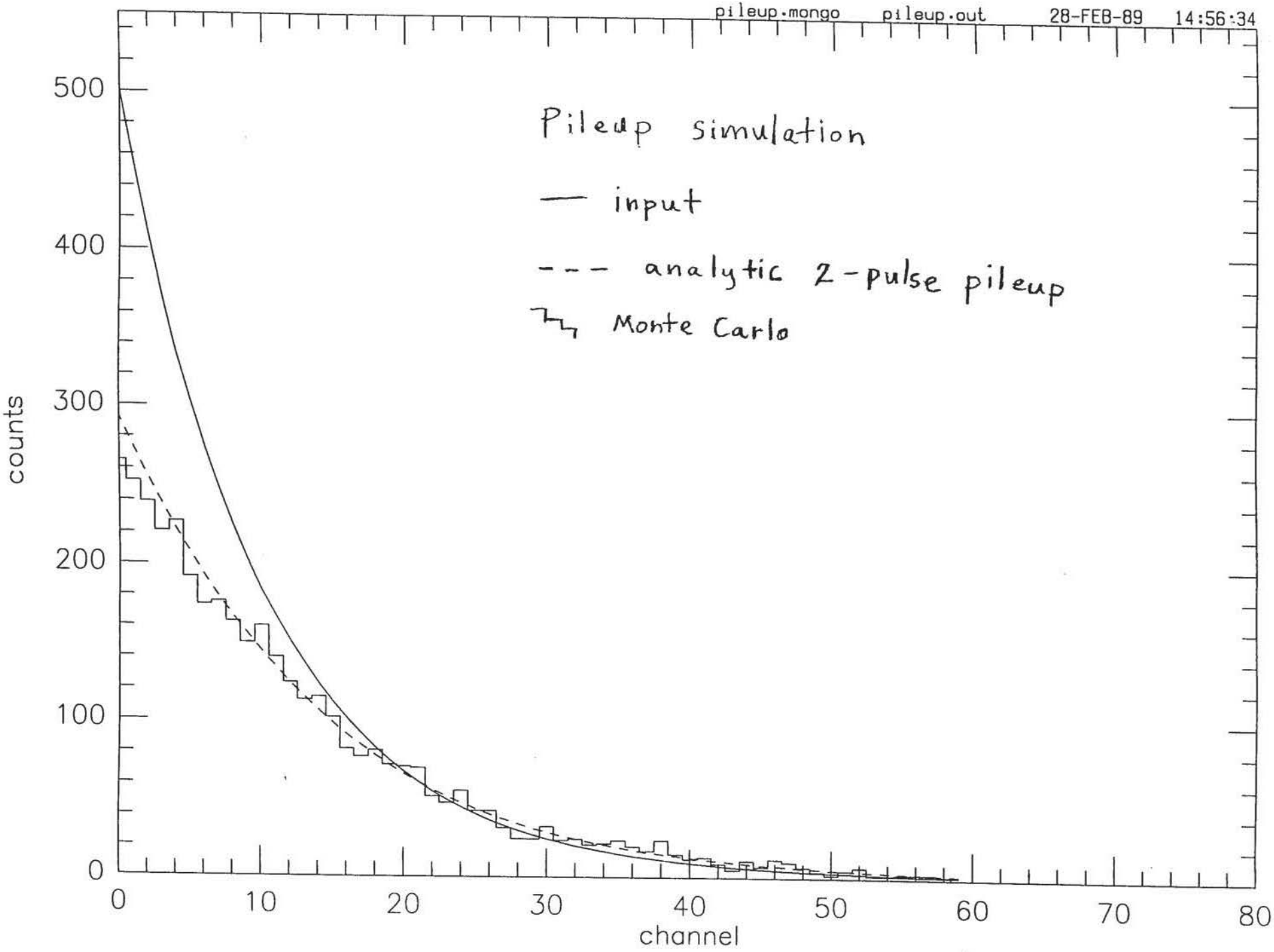
pileup.mongo pileup.out 28-FEB-89 14:56:34
Pileup simulation
input
analytic 2-pulse pileup
Monte Carlo
counts
channel
0
100
200
300
400
500
0
10
20
30
40
50
60
70
80

Figure 17